Supporting Information

Photothermal-Effect-Promoted Interfaced OH^- Filling and Conversion of Carrier Type in $(Co_{1-x}Ni_x)_3C$ During Water Oxidation

Xinzhi Ma[+], Mingyi Zhang[+], Fahad Azad, Qiong Gao, Zhikun Xu, Lin Li, Lili Wu, Xitian Zhang*, and Yujin Chen,**

Reagents and Materials. All chemicals including cobalt, nickel (purity, >99.99%; diameter, ~0.5 μm, Aladdin Chemical Co., Ltd.), active carbon powder (purity, >99.99%; ~0.5 μm, Aladdin Chemical Co., Ltd.), polyvinylidene fluoride (PVDF), and N-methylpyrrolidone (NMP) were of analytical grade and used without further purification. Hydrophilic and hydrophobic carbon papers were purchased from Toray Co., Ltd. Silver glue was acquired from CAIG Co., Ltd.

Synthesis of $(Co_{1-x}Ni_x)_3C$ (x=0, 0.1, and 0.2, respectively). The synthesis was mainly performed using a ball-milled method. Firstly, the cobalt and nickel powder and the pure active carbon were mixed with a mole ratio of 1:0:1, 0.9:0.1:1, and 0.8:0.2:1, using a planetary ball mill (Fritsch Pulverisette 4) with the ball-to-power weight ratio of 20:1. Before ball milling, the grinding bowls were "washed" with Ar (99.99%) through an inflation−deflation process to remove the inner air and then further vacuumed to decrease the inner pressure of bowls to 95 Kpa. The ball milling was carried out at a rotational speed of 900 rpm/min for 10 h. Then the products were collected.

Morpho-Structural Characterization. X-ray diffractometry was performed using a Rigaku D/max2600 X-ray diffractometer (XRD) with Cu-Kα radiation (λ = 1.54178 Å). The field-emission scanning electron microscopy (FE-SEM) micrographs were taken on a SU 70, Hitachi, Japan. The transmission electron microscopy (TEM) was performed on an FEI, Tecnai TF20 field-emission electron microscope, operated at an acceleration voltage of 200 kV. X-ray photoelectron spectra (XPS) were obtained on a Thermofisher Scientific Company X-ray photoelectron spectrometer using Mg Kα as the excitation source. Infrared images were taken using an infrared thermal imager HT-18, Hti.

Photoelectrochemical Investigations of OER. The photoelectrochemical OER measurements of $(Co_{1-x}Ni_x)_3C$ were carried out using a three-electrode system on a VMP3 electrochemical workstation (BioLogic, France) with a standard three-electrode water bath photoelectrochemical cell coupled with a temperature control system. This system contained a constant temperature water bath (HH-1, Shanghai Lichen Instrument Technology Co., Ltd) and a peristaltic pump (NKCP-C-B08B, Kamoer). The visible light source was obtained from a Xe-lamp-based solar simulator (CEL-HXF300 device, Beijing Zhongjiao Jinyuan Technology Co., Ltd.)

The as-obtained catalysts were respectively loaded on hydrophilic and hydrophobic carbon-fibre-paper electrodes (5×5 mm) with the same loading mass of 2 mg cm^{-2}. Typically, 20 mg catalysts mixed with 100 μL PVDF (5 wt%) solution were dispersed in 300 μL NMP solutions and sonicated for 60 min to form a homogeneous ink (~ 400 μL). Then, 10 μL dispersion solutions (~ 0.5 mg) were dropped onto the carbon-fibre-paper electrode. The carbon rod and Ag/AgCl (3M KCl saturated) were used as counter and reference electrodes. All the electrode potentials were referenced to Ag/AgCl reference electrode, which were converted to reversible hydrogen electrode (RHE) using the equation $E_{(RHE)} = E_{(Ag/AgCl)} + 0.059V \times pH + 0.198V$.

Variable Temperature Hall Effect of the Catalysts. For Variable Temperature Hall Effect measurements, 100 mg samples were previously conducted tabletting processing to form 10×10 mm flakes. On these flakes, 0.5 μL silver glue droplets were subsequently dropped on the four corners of the square piece to use as the electrodes. The devices were successfully obtained after a 2 hour vacuum drying process. The variable temperature Hall effect tests were conducted in four probes on a Nanometrics HL5500PC (America).

Photocurrent Response of the Catalysts. The substrates of photocurrent devices of these catalysts were silica glass, and all other preparation processes were the same as in the case of the electrodes used for OER measurements. Photocurrent-time curves of the $(Co_{1-x}Ni_x)_3C$ were performed on a light-current system containing a Xenon-lamp-based solar simulator and a computerized source meter (Keithley 2400). The data were collected in the dark and under illumination with visible light with a drain voltage of 2V.

Figures and Tables

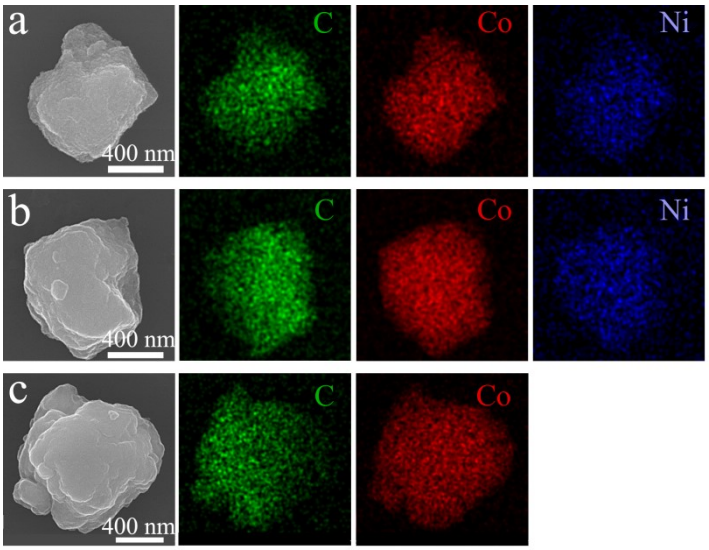

Figure S1. (a, b, and c) EDX mappings of $(Co_{0.8}Ni_{0.2})_3C$, $(Co_{0.9}Ni_{0.})_3C$, and Co_3C, respectively.

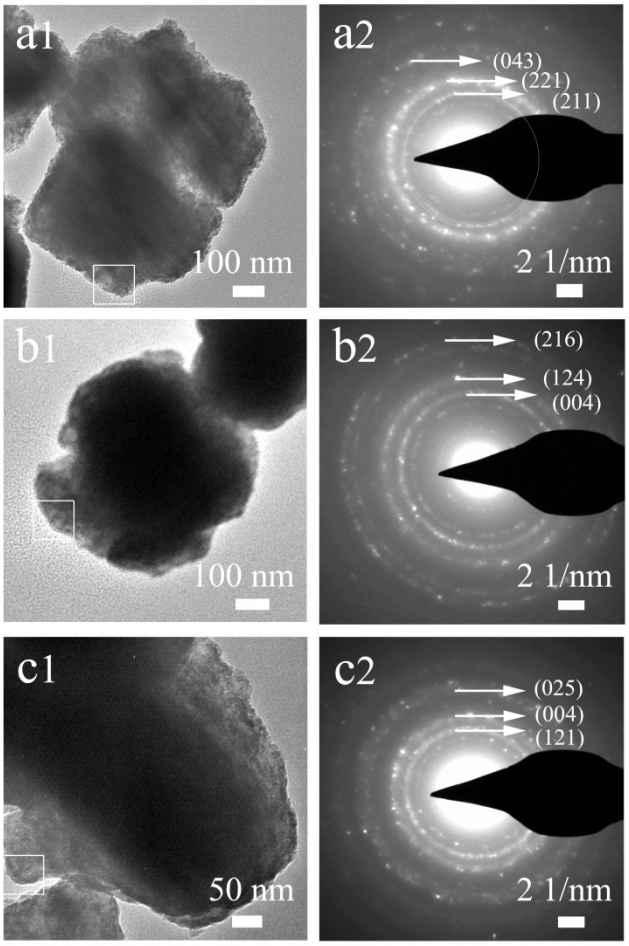

Figure S2. (a1-c1) TEM images of $(Co_{0.8}Ni_{0.2})_3C$, $(Co_{0.9}Ni_{0.})_3C$ and Co_3C, respectively; (a2-c2) SAED patterns of $(Co_{0.8}Ni_{0.2})_3C$, $(Co_{0.9}Ni_{0.})_3C$ and Co_3C, respectively.

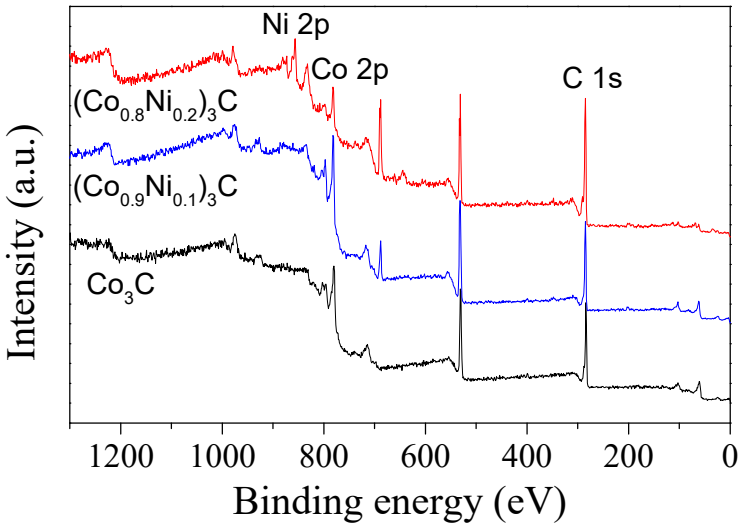

Figure S3. Survey XPS spectrum of Co_3C, $(Co_{0.9}Ni_{0.1})_3C$, and $(Co_{0.8}Ni_{0.2})_3C$, respectively.

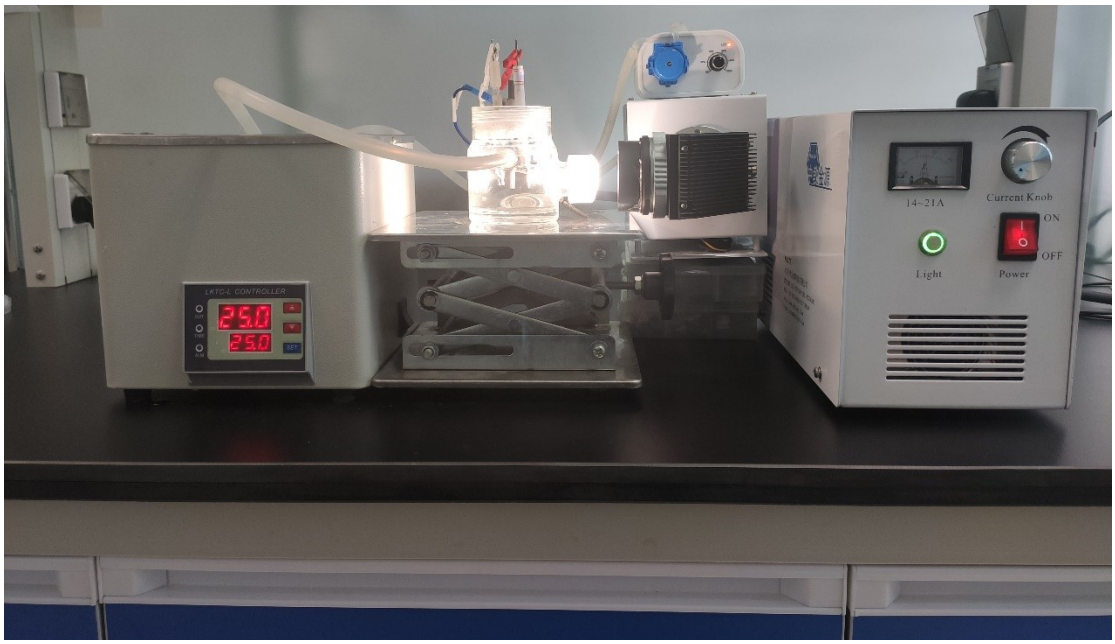

Figure S4 Digital photo of interfaced photothermal electrochemical device.

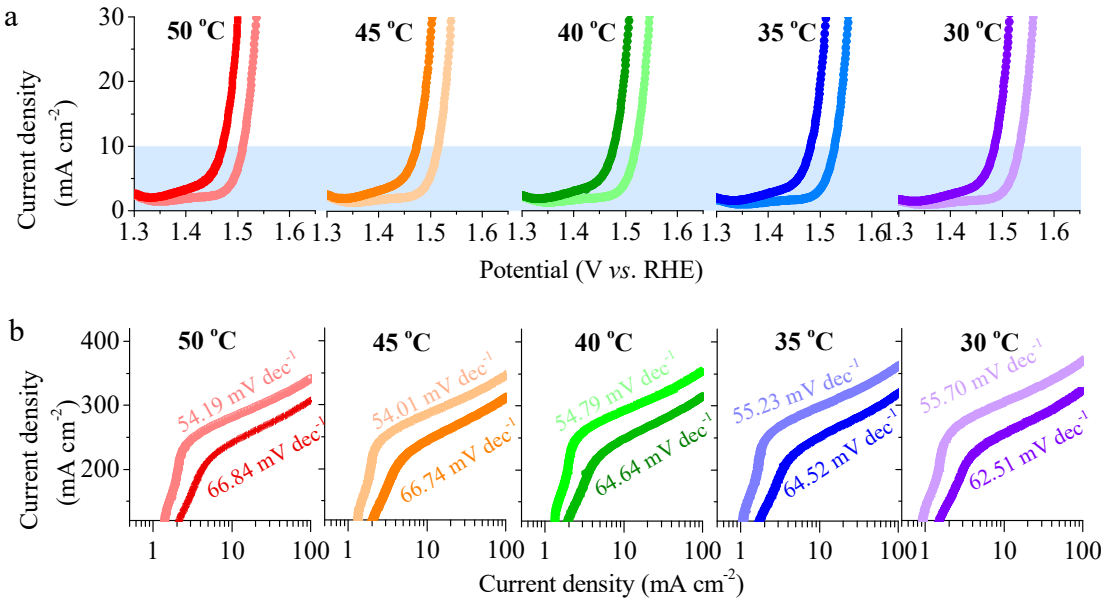

Figure S5. (a and b) LSVs and Tafel slopes of $(Co_{0.8}Ni_{0.2})_3C$ measured at variable temperatures from 25 to 50 °C without (light-colored line) and with (dark-colored line) CSI, respectively.

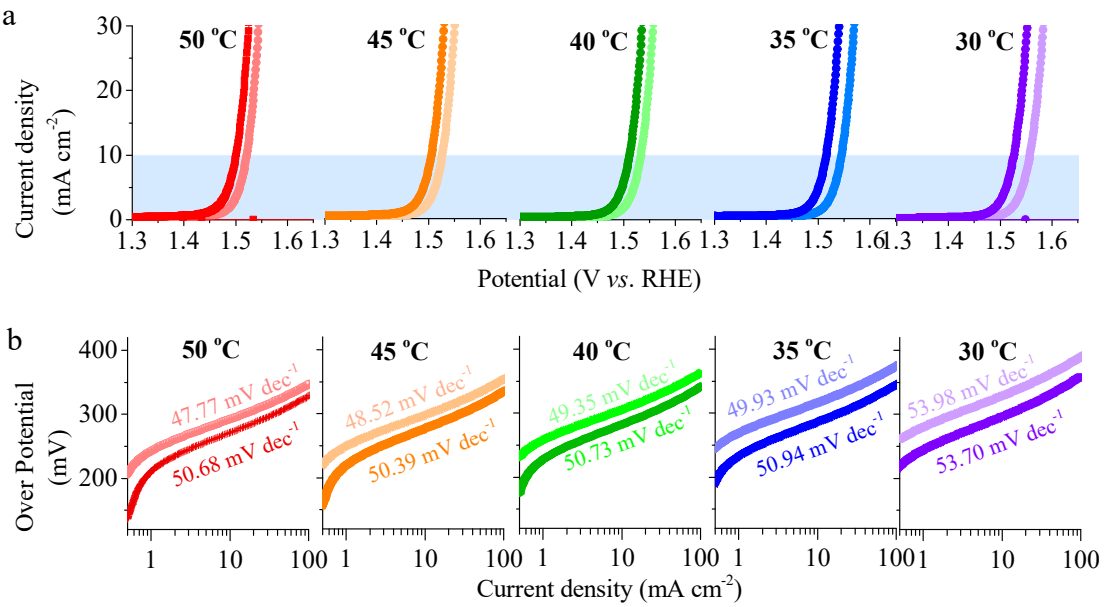

Figure S6. (a and b) LSVs and Tafel slopes of $(Co_{0.9}Ni_{0.1})_3C$ measured at variable temperatures from 25 to 50 °C without (light-colored line) and with (dark-colored line) CSI, respectively.

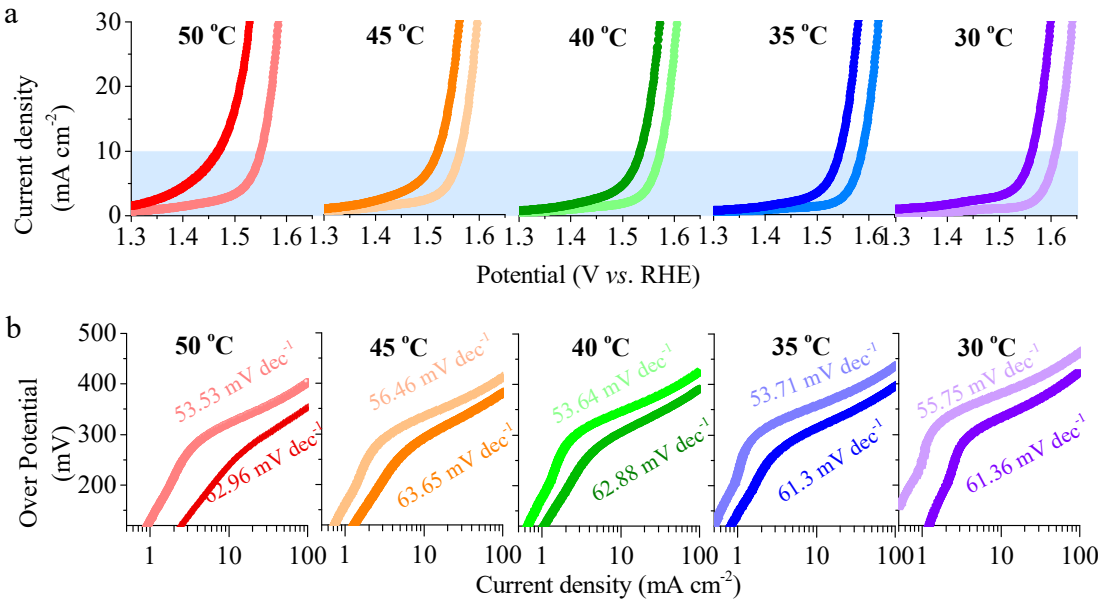

Figure S7. (a and b) LSVs and Tafel slopes of Co_3C measured at variable temperatures from 25 to 50 °C without (light-colored line) and with (dark-colored line) CSI, respectively.

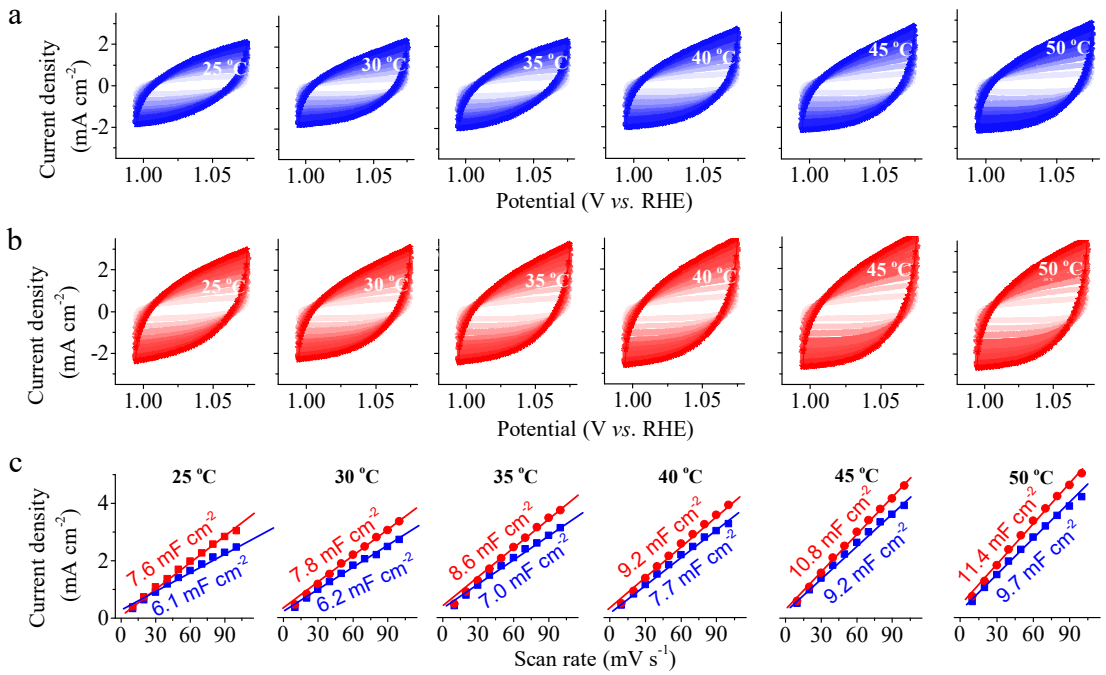

Figure S8. (a and b) CV curves of $(Co_{0.8}Ni_{0.2})_3C$ measured on the hydrophobic electrode at variable temperatures from 25 to 50 ℃ without and with light irradiation, respectively; (c) corresponding C_{dl} values, wherein red and blue lines are the values with and without CSI.

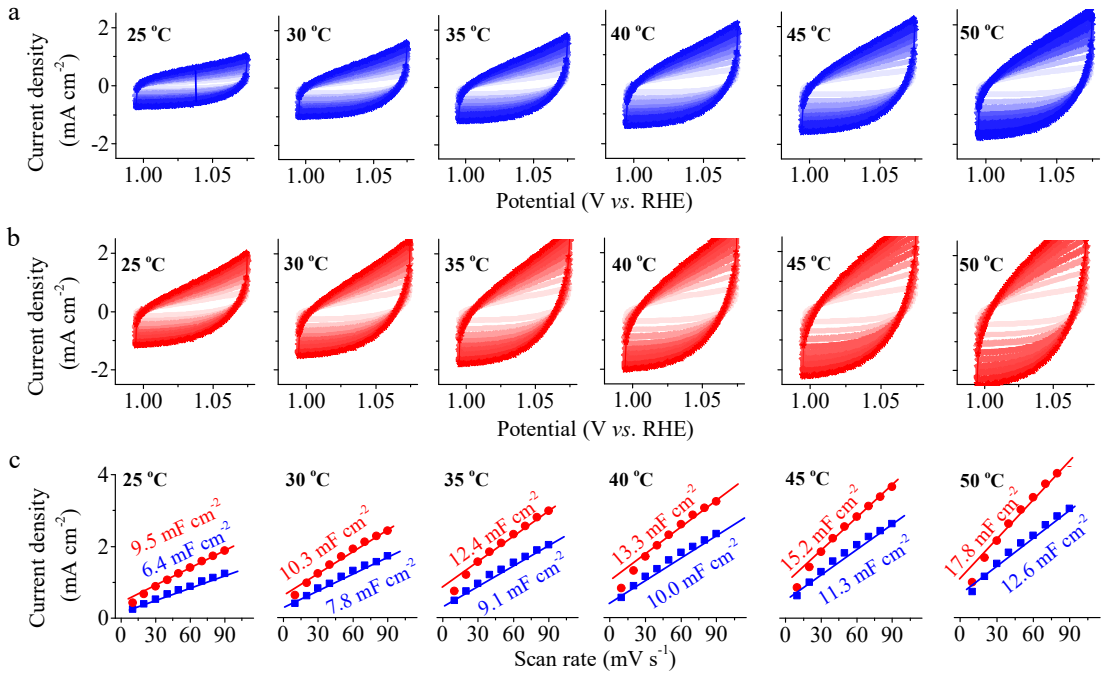

Figure S9. (a and b) CV curves of $(Co_{0.9}Ni_{0.1})_3C$ measured on the hydrophobic electrode at variable temperatures from 25 to 50 ℃ without and with light irradiation, respectively; (c) corresponding C_{dl} values, wherein red and blue lines are the values with and without CSI.

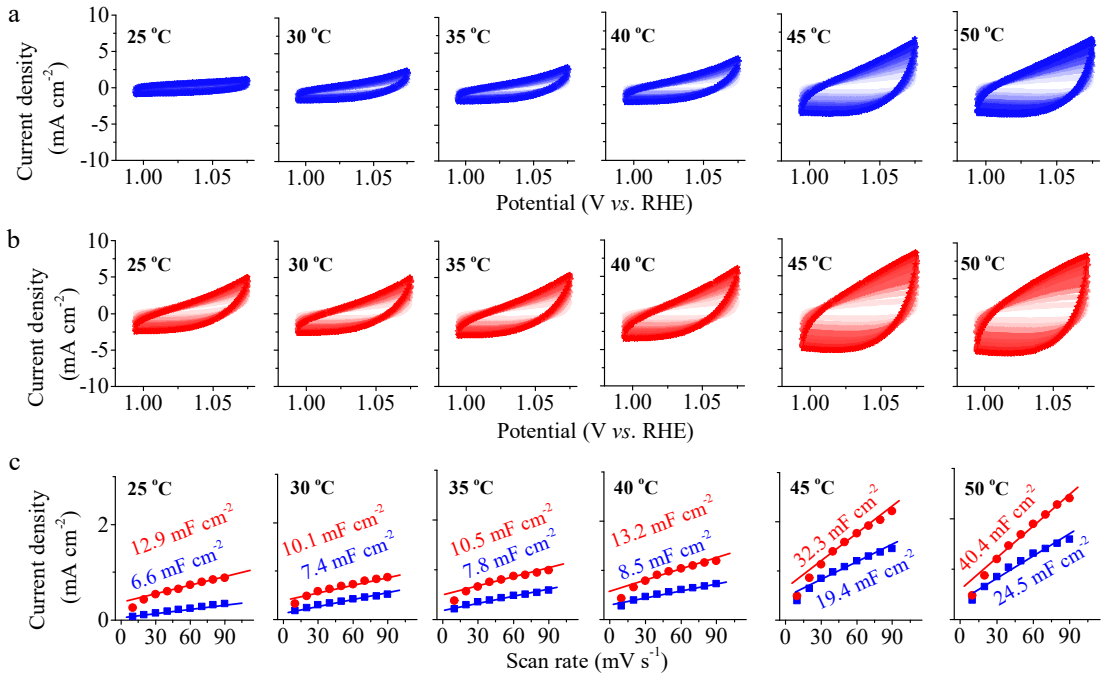

Figure S10. (a and b) CV curves of Co_3C measured on the hydrophobic electrode at variable temperatures from 25 to 50 °C without and with light irradiation, respectively; (c) corresponding C_{dl} values, wherein red and blue lines are the values with and without CSI.

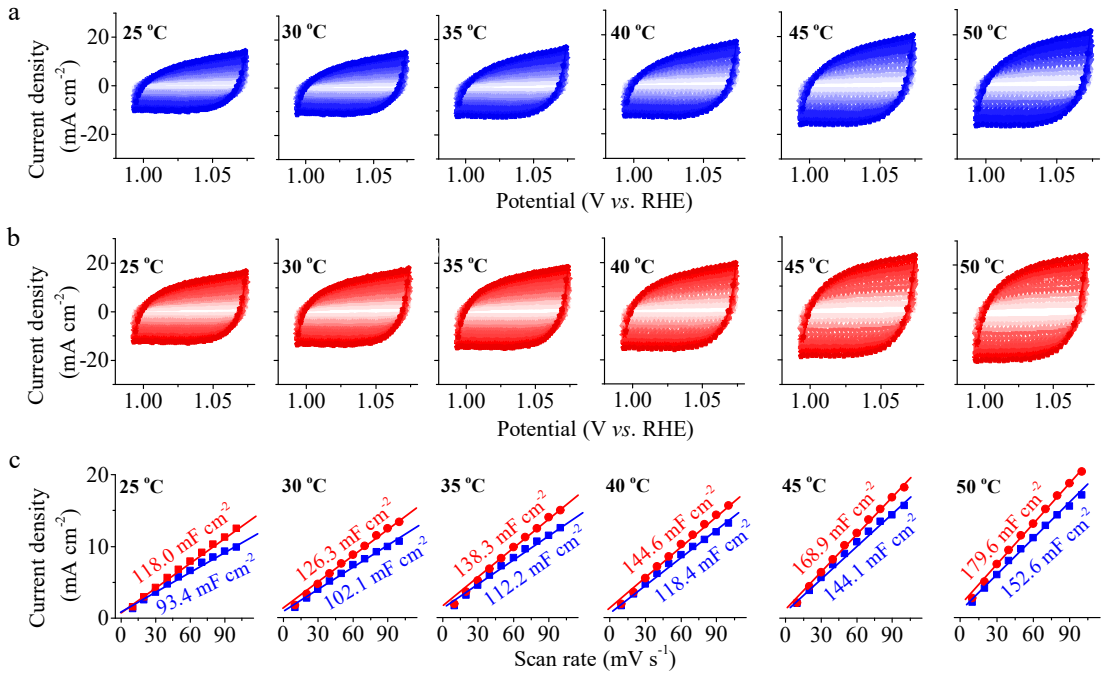

Figure S11. (a and b) CV curves of $(Co_{0.8}Ni_{0.2})_3C$ measured on the hydrophilic electrode at variable temperatures from 25 to 50 ℃ without and with light irradiation, respectively; (c) corresponding C_{dl} values, wherein red and blue lines are the values with and without CSI.

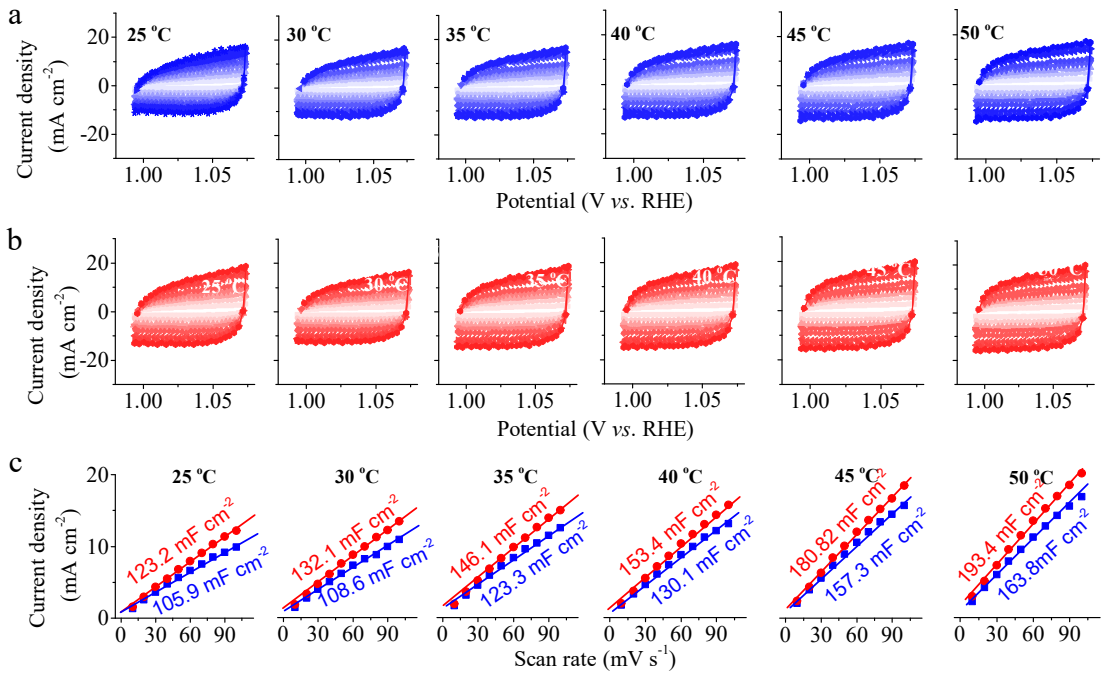

Figure S12. (a and b) CV curves of $(Co_{0.9}Ni_{0.1})_3C$ measured on the hydrophilic electrode at variable temperatures from 25 to 50 ℃ without and with light irradiation, respectively; (c) corresponding C_{dl} values, wherein red and blue lines are the values with and without CSI.

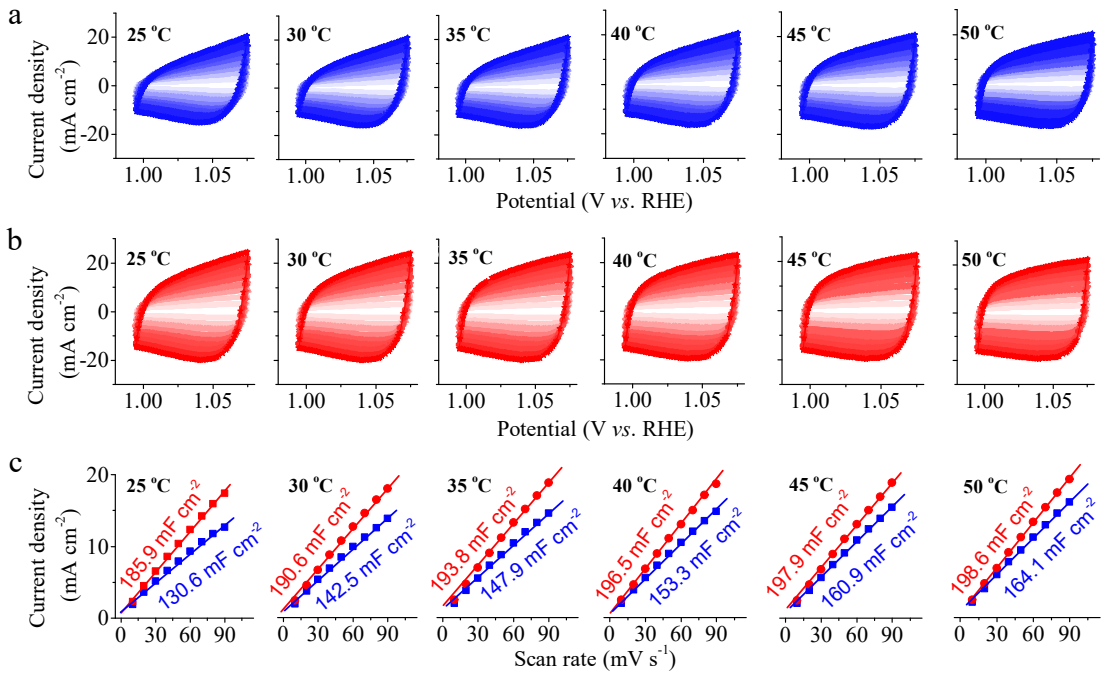

Figure S13 (a and b) CV curves of Co_3C measured on the hydrophilic electrode at variable temperatures from 25 to 50 °C without and with light irradiation, respectively; (c) corresponding C_{dl} values, wherein red and blue lines are the values with and without CSI.

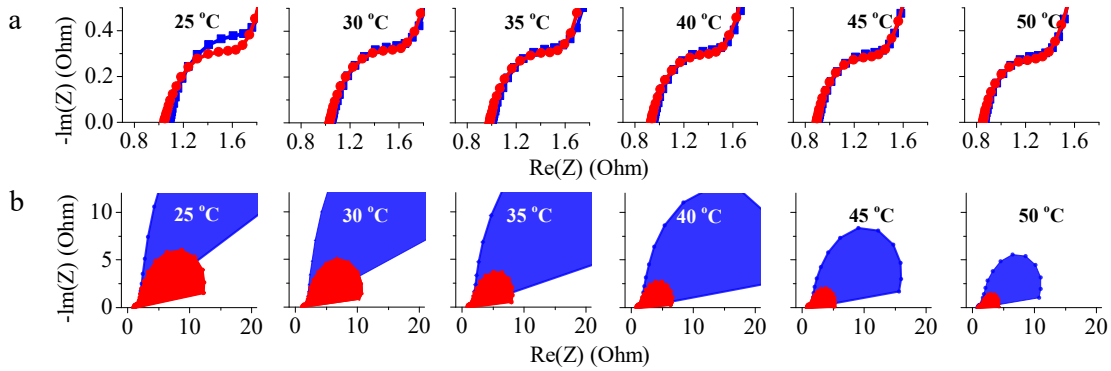

Figure S14 (a and b) R_{ct} and R_{mt} of $(Co_{0.8}Ni_{0.2})_3C$ measured at variable temperatures from 25 to 50℃ with (red lines) and without (blue lines) CSI.

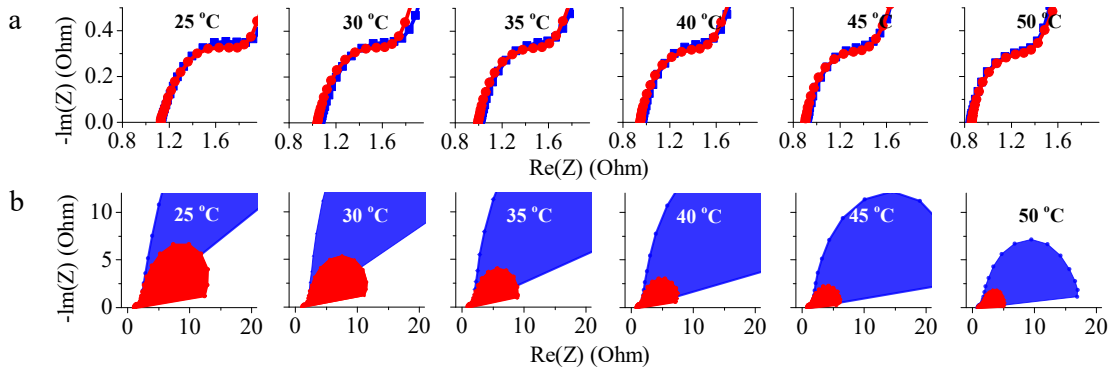

Figure S15 (a and b) R_{ct} and R_{mt} of $(Co_{0.9}Ni_{0.1})_3C$ measured at variable temperatures from 25 to 50℃ with (red lines) and without (blue lines) CSI.

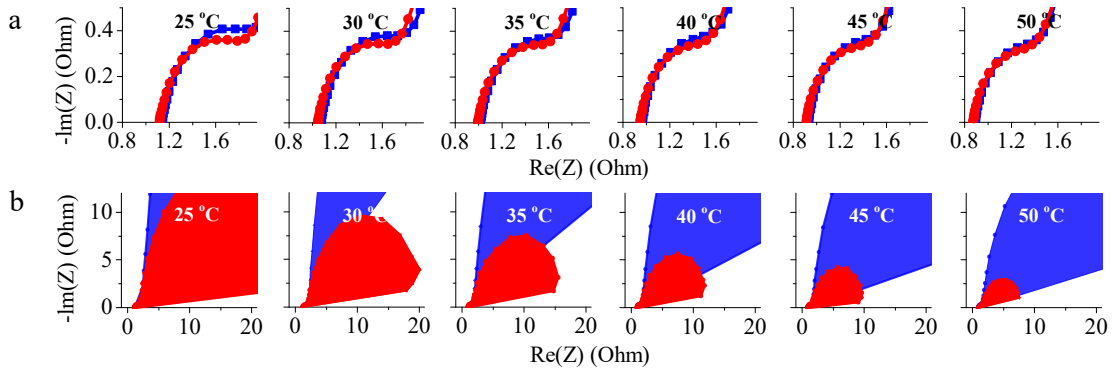

Figure S16 (a and b) R_{ct} and R_{mt} of Co_3C measured at variable temperatures from 25 to 50℃ with (red lines) and without (blue lines) CSI.

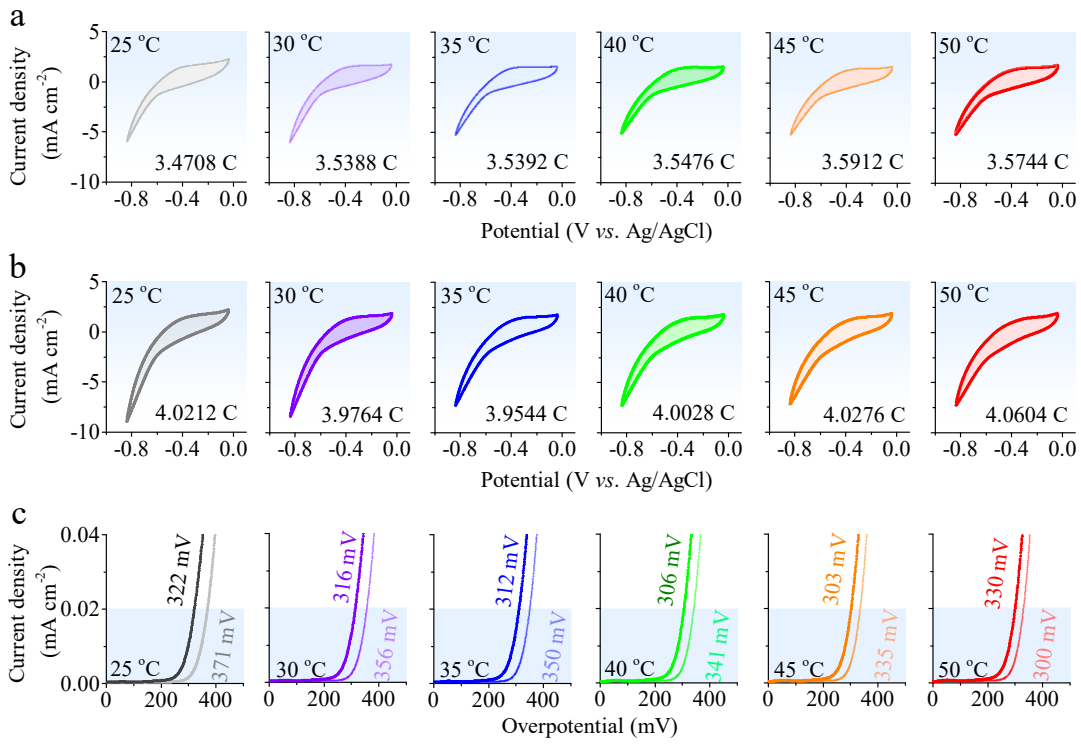

Figure S17 (a and b) Cyclic voltammetry cycling of $(Co_{0.8}Ni_{0.2})_3C$ in phosphate buffer (from 25 to 50 °C) with a scan rate of 50 mV s^{-1} range from -0.8 to 0 V *vs.* Ag/AgCl measured in dark and under CSI, respectively; and (c) TOF data calculated in dark (light-colored lines) and under CSI (dark-colored lines), respectively.

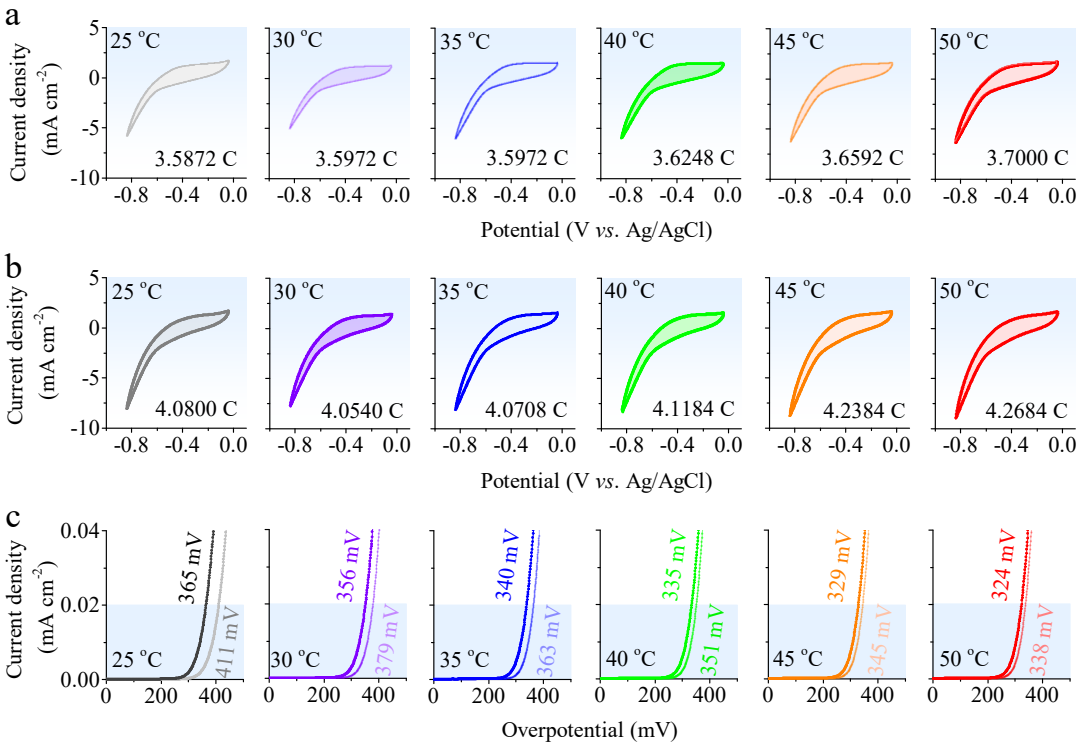

Figure S18 (a and b) Cyclic voltammetry cycling of $(Co_{0.9}Ni_{0.1})_3C$ in phosphate buffer (from 25 to 50 °C) with a scan rate of 50 mV s^{-1} range from -0.8 to 0 V *vs.* Ag/AgCl measured in dark and under CSI, respectively; and (c) TOF data calculated in dark (light-colored lines) and under CSI (dark-colored lines), respectively.

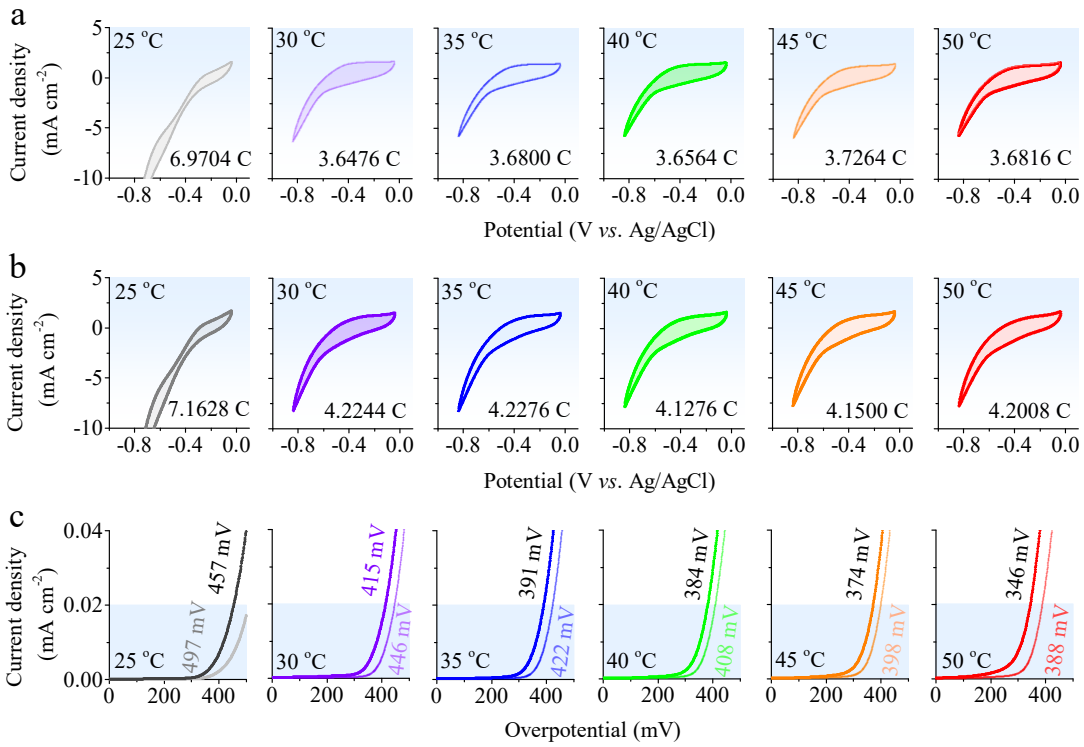

Figure S19 (a and b) Cyclic voltammetry cycling of Co_3C in phosphate buffer (from 25 to 50 °C) with a scan rate of 50 mV s^{-1} range from -0.8 to 0 V *vs*. Ag/AgCl measured in dark and under CSI, respectively; and (c) TOF data calculated in dark (light-colored lines) and under CSI (dark-colored lines), respectively.

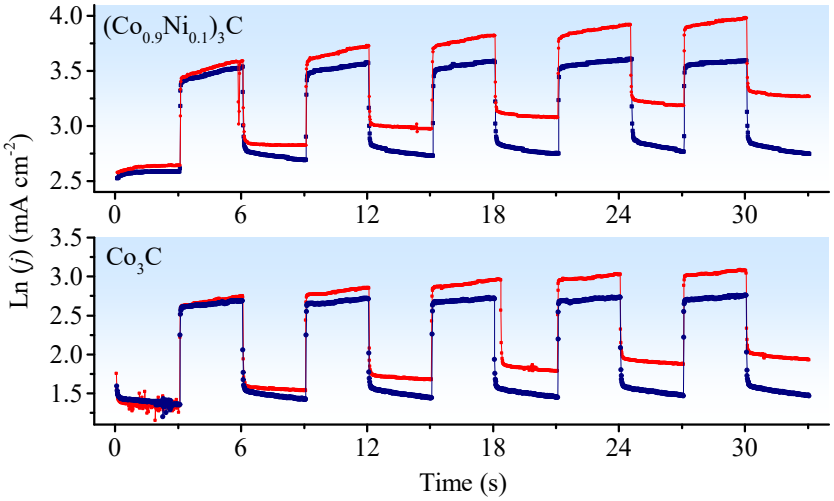

Figure S20 Photoelectrochemical OER responses of $(Co_{0.9}Ni_{0.1})_3C$ and Co_3C measured under TC (blue lines) and TNW (red lines) conditions at 1.58 V (*vs*. RHE).

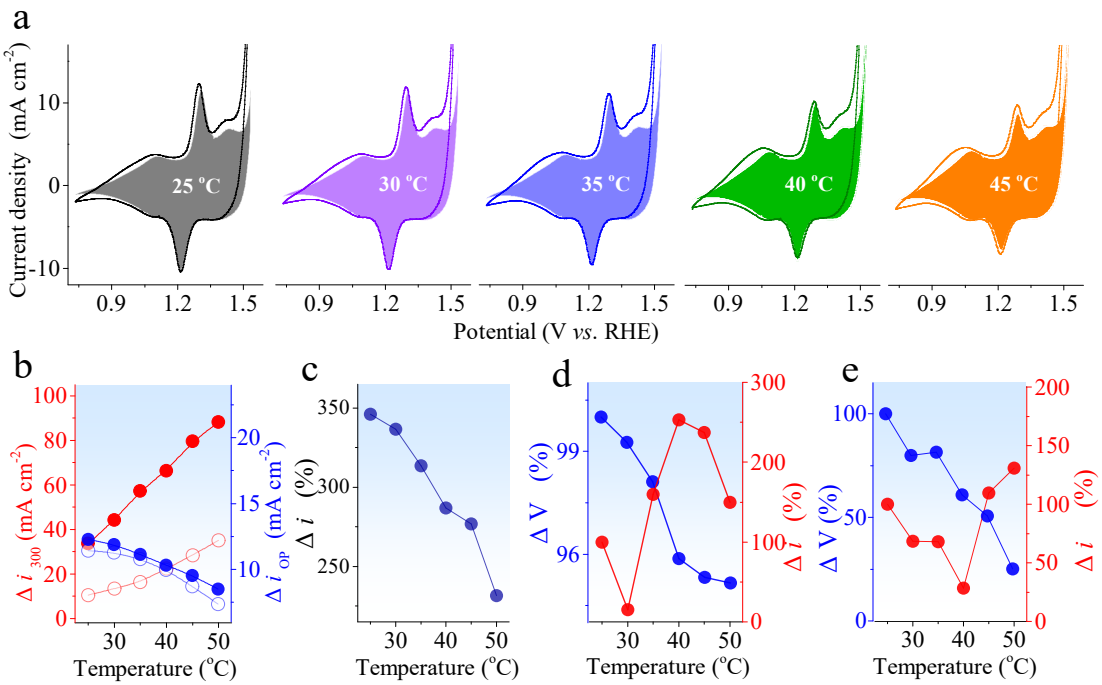

Figure S21 (a) CVs of $(Co_{0.9}Ni_{0.1})_3C$ measured at different temperatures from 25 to 50 °C with (hollow) and without (solid) light irradiation; (b) relationships between the oxide peak intensities (Δi_{OP}) of metal$^{2+/3+}$ (blue) and current densities (Δi_{300}) measured at the overpotential of 300 mV (red), with (solid) and without (hollow) light irradiation; (c, d, and e) temperature dependences of intensity increment, amount (red) and potential range (blue) of Co/Ni$^{+2/+3}$ redox peaks, and amount (red) and potential range (blue) of redox peaks of absorbed O-related species of $(Co_{0.9}Ni_{0.1})_3C$ as light irradiated, related to the values measured at 25 °C.

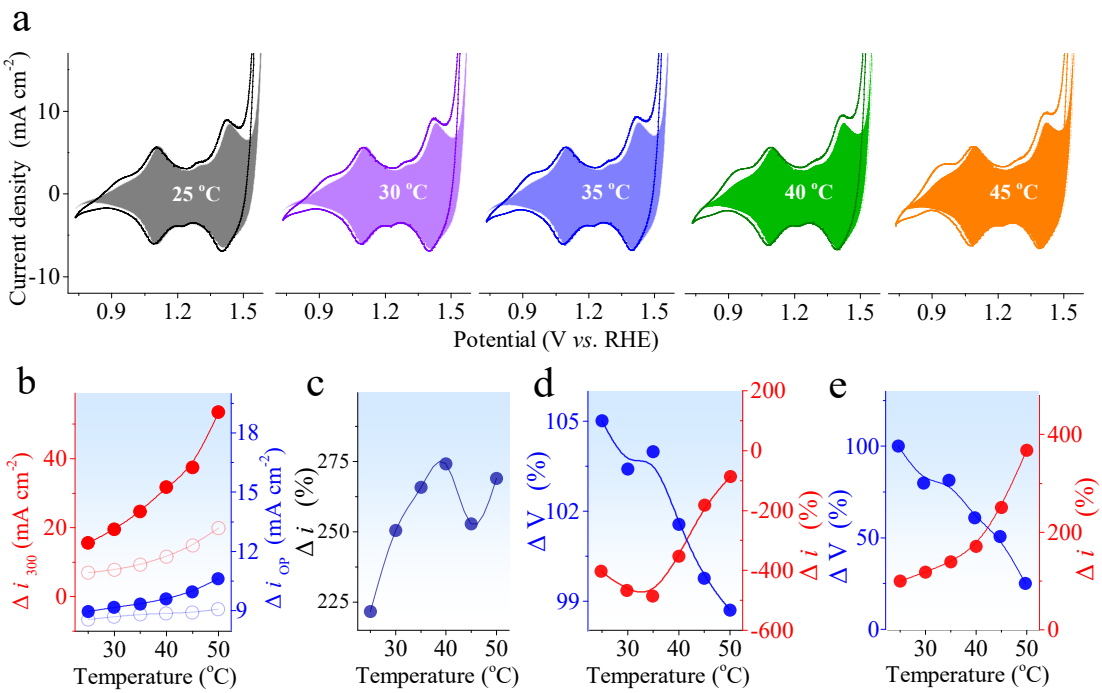

Figure S22 (a) CVs of Co_3C measured at different temperatures from 25 to 50 °C with (hollow) and without (solid) light irradiation; (b) relationships between the oxide peak intensities (Δi_{OP}) of metal$^{2+/3+}$ (blue) and current densities (Δi_{300}) measured at the overpotential of 300 mV (red), with (solid) and without (hollow) light irradiation; (c, d, and e) temperature dependences of intensity increment, amount (red) and potential range (blue) of $Co^{+2/+3}$ redox peaks, and amount (red) and potential range (blue) of redox peaks of absorbed O-related species of Co_3C as light irradiated, related to the values measured at 25 °C.

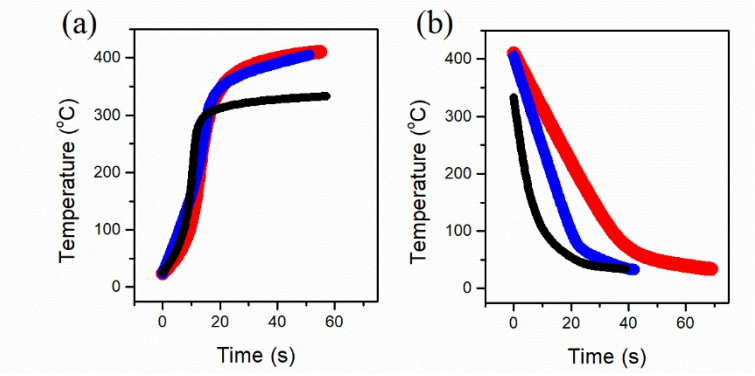

Figure S23 Temperature dependence of $(Co_{0.8}Ni_{0.2})_3C$ (red), $(Co_{0.9}Ni_{0.1})_3C$ (blue), and Co_3C (black) on photothermal conversion. (a) CSI; (b) without CSI.

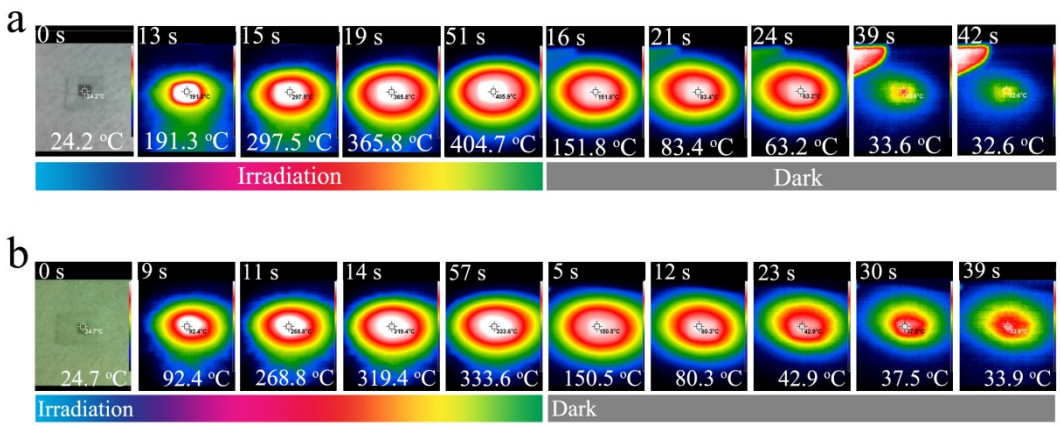

Figure S24 (a and b) Infrared images taken in dark and CSI conditions of $(Co_{0.9}Ni_{0.1})_3C$ and Co_3C, respectively.

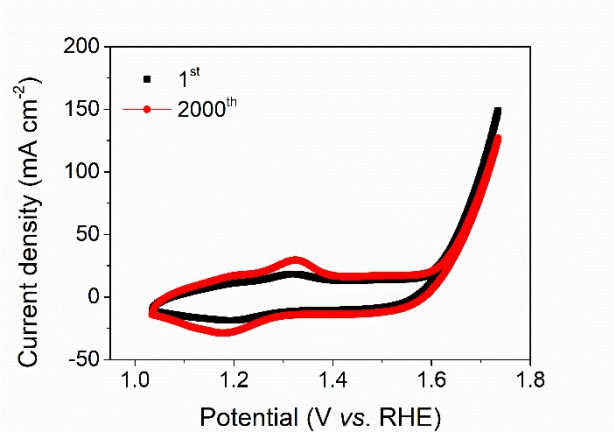

Figure S25 Durability test of $(Co_{0.8}Ni_{0.2})_3C$.

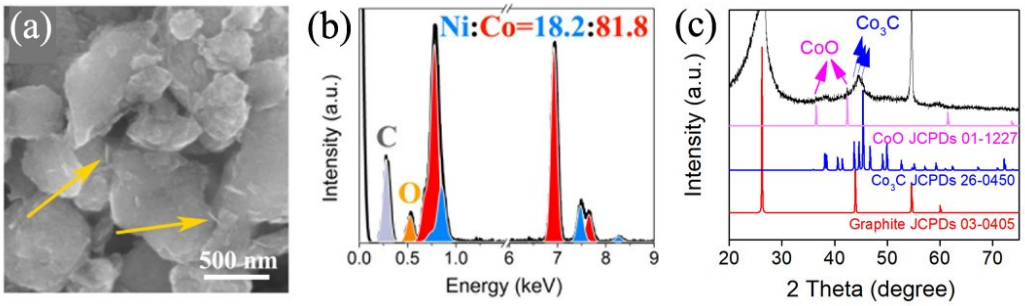

Figure S26 Structural information of $(Co_{0.8}Ni_{0.2})_3C$ after 2000 OER CVs. (a) SEM images, (b) corresponding EDS data, (c) XRD data.

Table S1 Comparison of OER activity of our $(Co_{0.8}Ni_{0.2})_3C$ catalyst with those of the OER catalysts reported previously.

Catalysts	KOH (M)	Tafel slope (mV dec^{-1})	Overpotential at 10mA cm^{-2} (mV)	Refs
Ni–Ni_3C/CC	1	43.8	268	*Small* **2020**, *16*, 2001642
Co_6W_6C@NC/CC	1	53.9	286	*Small* **2020**, *16*, 1907556
$Co_6Mo_6C_2$@NCNT-800	1	48.3	360	*J. Colloid Interf. Sci.* **2020**, *575*, 69–77

Fe_3C@Fe,N,S-GCM	0.1	253.8	327	*Carbon* **2019**, *150*, 93–100
Ni_3C/NC nanoflakes	1	72.0	309	*Electrochim. Acta* **2019,** *320*, 134631
0.5-Ni/Ni_3C@NCNT	1	58.0	280	*Electrochim. Acta* **2020**, *341*, 136032
Co-Ni_3C/Ni@C	1	67.7	325	*Hydrogen Energ.* **2019**, *44*, 24572–24579
Co-NC@Mo_2C	1	61.0	347	*Nano Energy* **2019**, *57*, 746–752
Co-Mo_2C NPs	0.1	38.0	347	*Appl. Catal. B–Environ.* **2018**, 227, 340–348
FCC@CNOs/NF	1	48.9	271	*Appl. Catal. B–Environ.* **2020**, *268*, 118385
Mo_2Co_1@N-CNS/CNT	1	74.4	300	*Chinese J. Catal.* **2019**, *40*, 1532–1359
Fe_3C@NG800-0.2	0.1	62.0	361	*ACS Appl. Mater. Inter.* **2015**, *7*, 21511–21520
Ni−Mo_xC/NC/CNT-100	1	74.0	328	*ACS Appl. Mater. Inter.* **2018**, *10*, 35025–35038
Ni/Ni_3C	0.1	57.6	350	*ACS Appl. Mater. Inter.* **2018**, *10*, 17827–17834
Co−Mo_2C@NCNT	1	-	377	*ACS Sustain. Chem. Eng.* **2018**, 6, 9912–9920
FeNC–S–Fe_xC/Fe	1	-	320	*Adv. Mater.* **2018**, *30*, 1804504
Co/N-CNTs@Ti_3C_2Tx	0.1	79.1	411	*Adv. Mater. Interfaces* **2018**, *5*, 1800392
$(MoS_2)_{0.125}Mo_2C$	0.1	209.0	280	*Adv. Mater. Interfaces* **2019**, *6*, 1900948
FeS/Fe_3C@N-S-C-800	1	81.0	570	*Adv. Funct. Mater.* **2018**, *28*, 1803973

Ni/Mo_2C(1:2)-NCNFs	1	78.4	288	*Adv. Energy Mater.* **2019**, *9*, 1803185
Fe-Ni_3C-2%	1	62.0	275	*Angew. Chem. Int. Ed.* **2017**, *56*, 12566–12570
Mo_2CMCNFs-1	1	68.0	320	*Chem Asian J.* **2020**, *15*, 1957–1962
Fe/Fe_3C@N-graphitic layer	0.1	-	770	*Green Chem.* **2016**, *18*, 427–432
Co_4Mo_2@NC	1	46.1	330	*J. Mater. Chem. A* **2017**, *5*, 16929–16935
Fe_3C@NCNTs-NCNFs	1	53.0	284	*J. Mater. Chem. A* **2017**, *5*, 19672–19679
$Co_{0.1}$-β-Mo_2C@NC	1	28.8	262	*Chem. Commun.* **2019**, *55*, 9995–9998
Co/Mo_2C-NCNTs	1	72.4	310	*ChemCatChem* **2020**, *12*, 3737–3745
Fe/Fe_3C@NCNT-750	0.1	176.0	390	*ChemElectroChem* **2018,** *5*, 471–477
Co-Bi/Ti_3C_2Tx	1	53.0	250	*ChemSusChem* **2018**, *11*, 3758–3765
Co/W-C@NCNSs(800)	1	75.5	323	*Energy Technol.* **2019**, *7*, 1800969